Analysis of sensitivity in quantitative micro-elastography

Jiayue Li,[1,2,3,*] **Matt S. Hepburn,**[1,2] (iD) **Lixin Chin,**[1,2] **Alireza Mowla,**[1,2] **and Brendan F. Kennedy**[1,2,3]

[1]*BRITElab, Harry Perkins Institute of Medical Research, QEII Medical Centre, Nedlands, Western Australia, 6009, Australia and Centre for Medical Research, The University of Western Australia, Crawley, Western Australia, 6009, Australia*

[2]*Department of Electrical, Electronic and Computer Engineering, School of Engineering, The University of Western Australia, 35, Stirling Highway, Perth, Western Australia, 6009, Australia*

[3]*Australian Research Council Centre for Personalized Therapeutics Technologies, Australia*

[*]*jiayue.li@research.uwa.edu.au*

Abstract: Quantitative micro-elastography (QME), a variant of compression optical coherence elastography (OCE), is a technique to image tissue elasticity on the microscale. QME has been proposed for a range of applications, most notably tumor margin assessment in breast-conserving surgery. However, QME sensitivity, a key imaging metric, has yet to be systematically analyzed. Consequently, it is difficult to optimize imaging performance and to assess the potential of QME in new application areas. To address this, we present a framework for analyzing sensitivity that incorporates the three main steps in QME image formation: mechanical deformation, its detection using optical coherence tomography (OCT), and signal processing used to estimate elasticity. Firstly, we present an analytical model of QME sensitivity, validated by experimental data, and demonstrate that sub-kPa elasticity sensitivity can be achieved in QME. Using silicone phantoms, we demonstrate that sensitivity is dependent on friction, OCT focus depth, and averaging methods in signal processing. For the first time, we show that whilst lubrication of layer improves accuracy by reducing surface friction, it reduces sensitivity due to the time-dependent effect of lubricant exudation from the layer boundaries resulting in increased friction. Furthermore, we demonstrate how signal processing in QME provides a trade-off between sensitivity and resolution that can be used to optimize imaging performance. We believe that our framework to analyze sensitivity can help to sustain the development of QME and, also, that it can be readily adapted to other OCE techniques.

1. Introduction

Quantitative micro-elastography (QME) is an emerging technique to map tissue elasticity into micro-scale images, termed micro-elastograms. QME is an extension of compression optical coherence elastography (OCE) which utilizes a pre-characterized compliant layer to measure the stress at the sample surface [1]. The measured two-dimensional (2-D) stress is then combined with three-dimensional (3-D) axial strain measurements to provide an estimation of 3-D elasticity, under the assumption that the axial stress is uniformly distributed with depth [2]. The main determinants of micro-elastogram formation in QME are the deformation of both the compliant layer and the sample, the measurement of this deformation (*i.e.*, displacement) using phase-sensitive optical coherence tomography (OCT), and the signal processing used to convert measured displacement to elasticity. Initial demonstrations of QME have shown promise, particularly in breast tumor margin assessment [3,4] and mechanobiology [5–7]. Of note, a recent study demonstrated that QME has a sensitivity of 93% and a specificity of 96% in detecting tumor within 1 mm of the boundaries of specimens excised during breast-conserving surgery [4].

To enable future translation to clinical and biological applications, QME has been incorporated in both endoscopic [8] and handheld probe [9,10] configurations.

The development of QME, and of OCE more generally, has been expedited by systematic studies of strain estimation methods [11–15] and key imaging parameters, such as image contrast [16,17] and spatial resolution [18–20]. However, elasticity sensitivity (*i.e.*, the minimum measurable variation in elasticity) [9], has yet to be formally analyzed. Prior studies have investigated sensitivity to some degree [6,11,12]. In particular, a recent QME study has introduced a method for measuring elasticity sensitivity as the standard deviation of elasticity at the same spatial location over time. However, the lack of a systematic analysis of sensitivity, and the system parameters that determine it, makes it challenging to optimize QME for given applications and to determine the suitability of QME in new application areas. As a result, it is currently unclear what variation in sample elasticity is required, in a given imaging configuration, to distinguish features within samples of interest. Moreover, the absence of a thorough analysis of sensitivity makes it challenging to generate micro-elastograms with similar image quality between different imaging systems and even between the same imaging system at different time points.

A main limitation of previous, preliminary definitions of QME sensitivity is that it has largely been assumed that the primary determinant of elasticity sensitivity is OCT signal-to-noise ratio (SNR), owing to the relationship between OCT SNR and displacement sensitivity in phase-sensitive OCT [21]. Given that micro-elastogram formation is also determined by mechanical deformation and signal processing, it is clear that a broader consideration of image formation is necessary to provide a comprehensive analysis of sensitivity in QME. To address this, in this paper, we present the first framework to analyze QME sensitivity. To provide a theoretical basis for our analysis, we present an analytical model of elasticity sensitivity that incorporates mechanical deformation, OCT SNR and the signal processing used to estimate elasticity. This model describes the precision, *i.e.*, standard deviation, of the elasticity measurement over time at a single location, analogous to previous definitions of OCE displacement [11,22,23] and strain sensitivity [11,16,23]. In this study, we term this measurement the *QME system sensitivity*. We validate our model of the system sensitivity through close correspondence with experimental data acquired from a homogeneous, scattering phantom. We then utilize our framework to assess the contribution to the system sensitivity of friction (a characteristic of mechanical deformation), focus position (a characteristic of the OCT system), and temporal and spatial averaging (characteristics of the signal processing). To assess the relationship between sensitivity and accuracy, we also present experimental results showing the effect of both lubrication and compliant layer thickness on the accuracy of the elasticity measurement. Lastly, we consider the spatial dependence in sensitivity within a micro-elastogram brought about by both OCT speckle and mechanical heterogeneity. The former modulates the OCT SNR throughout micro-elastograms, and the latter can lead to large variations in elasticity in regions adjacent to features within micro-elastograms. To distinguish these effects from QME system sensitivity, we define spatially varying sensitivity as *QME feature sensitivity*. We reconcile feature sensitivity and system sensitivity experimentally by demonstrating how feature sensitivity can be improved to match system sensitivity by trading off resolution through spatial averaging. We believe that this framework provides a tool to optimize the imaging parameters in QME and that this framework could readily be adapted to evaluate other variants of OCE.

2. Theory: elasticity in QME

Following the precedent set in prior elastography techniques, to enable QME to be performed in a practical timeframe, and to facilitate straightforward interpretation of micro-elastograms, it is commonly assumed that samples are both linearly elastic, and isotropic [24–26]. In this case, the measured elasticity, E_{sample} is equal to the Young's modulus, which is defined as the ratio of the uniaxial stress imparted to the sample, σ_{sample}, to the resultant normal strain in the sample along

the same axis, ε_{sample}:

$$E_{sample} = \frac{\sigma_{sample}}{\varepsilon_{sample}}. \tag{1}$$

For samples undergoing uniaxial compression, bulk axial strain is defined as the ratio of the change in length to the initial length, $\Delta l/l$. In OCE, the depth-resolved local strain is defined to describe the strain distribution within the sample [27]:

$$\varepsilon_{sample}(z) = \frac{\Delta d_{sample}(z)}{\Delta z}, \tag{2}$$

where $\Delta d_{sample}(z)$ is the change of displacement over the depth, Δz, in the sample.

The stress at the sample surface can be determined using a compliant silicone layer which is considered as a system component of QME, with known stress-strain relationship, placed on top of the sample [1–4,6,9,28]. At each lateral position, the strain in the layer is measured using OCT, and is converted to a measurement of surface stress using the pre-calibrated stress-strain curve of the compliant layer. The layer and sample can be approximated as a simple one-dimensional (1-D) spring system coupled in series [29]. Stress is, thus, assumed to be uniaxial and uniform with depth, such that the stress in the layer is assumed to be equal to the stress distributed throughout the sample. Hence, σ_{sample} in Eq. (1) can be replaced by σ_{layer}, which is calculated from the product of ε_{layer}, the local strain in the layer, and the gradient of the stress-strain curve at the given pre-strain, $E_{layer}(\varepsilon_{pre-strain})$, where "pre-strain" refers to the bulk strain imparted to the layer-sample system to ensure uniform contact prior to imparting a local strain from a ring actuator [2,3,23,30]:

$$\sigma_{layer} = E_{layer}(\varepsilon_{pre-strain}) \times \varepsilon_{layer}. \tag{3}$$

In this study, ε_{layer} is calculated from the displacement measured at the layer-sample interface, d_{layer}, divided by the layer thickness at a given pre-strain, $l_{layer}(\varepsilon_{pre-strain})$, measured from the edge detection in OCT [2]:

$$\varepsilon_{layer} = \frac{d_{layer}}{l_{layer}(\varepsilon_{pre-strain})}. \tag{4}$$

Then, the depth-resolved elasticity of the sample, $E_{sample}(z)$ can be estimated by substituting Eqs. (2)–(4) in Eq. (1):

$$E_{sample}(z) \approx \frac{\sigma_{layer}}{\varepsilon_{sample}(z)} = \frac{E_{layer}(\varepsilon_{pre-strain})}{l_{layer}(\varepsilon_{pre-strain})} \frac{d_{layer}}{\varepsilon_{sample}(z)}. \tag{5}$$

2.1. QME system sensitivity

In this section, we present an analytical model for QME system sensitivity, which we define as the variability in elasticity values measured from the same location over time, determining the minimum measurable change in elasticity that a given QME system can distinguish from noise. Our model incorporates parameters of mechanical deformation, OCT and signal processing. We achieve this by defining displacement sensitivity, strain sensitivity, stress sensitivity and elasticity (system) sensitivity, respectively.

2.1.1. Displacement sensitivity

In phase-sensitive QME, the depth-resolved axial displacement within the sample, $d_{sample}(z)$, is calculated from the phase difference, $\Delta\phi_{sample}(z)$, between unloaded and loaded complex OCT B-scans [22,31]:

$$d_{sample}(z) = \frac{\lambda\Delta\phi_{sample}(z)}{4\pi n_{sample}}, \tag{6}$$

where λ is the central wavelength of the light source and n_{sample} is the refractive index of the sample. Similarly, the axial displacement of the layer measured at the interface between the

sample and the layer, d_{layer}, is calculated from $\Delta\phi_{layer}$:

$$d_{layer} = \frac{\lambda\Delta\phi_{layer}}{4\pi n_{layer}}, \tag{7}$$

where n_{layer} is the refractive index of the layer. However, phase difference is a circular variable, and hence requires phase unwrapping to disambiguate the displacement calculation, which is a linear variable [32]. To simplify this, in our model, we assume that any phase unwrapping is "perfect" and introduces no further noise into the measurement. We assume that the optical noise can be modelled as additive Gaussian white noise [33,34]. Further assuming that the OCT SNR >> 1, then the phase difference sensitivity, $s_{\Delta\phi}$, is approximated by [21]:

$$s_{\Delta\phi} = \frac{1}{\sqrt{SNR_{OCT}}}. \tag{8}$$

By temporally averaging N complex OCT B-scans, the phase difference sensitivity is improved by a factor of $1/\sqrt{N}$ [33,35]. Combining Eqs. (6) and (7) with Eq. (8) and incorporating temporal averaging (N), the displacement sensitivity in the sample and layer, respectively, are expressed as:

$$s_{d,sample}(z) = \frac{\lambda}{4\pi n_{sample}\sqrt{SNR_{OCT,sample}(z) \times N}}, \tag{9}$$

$$s_{d,layer} = \frac{\lambda}{4\pi n_{layer}\sqrt{SNR_{OCT,layer}N}}, \tag{10}$$

where $SNR_{OCT,sample}(z)$ is the OCT SNR detected in the sample at depth z, and $SNR_{OCT,layer}$ is the OCT SNR detected at the layer-sample interface.

2.1.2. Strain sensitivity

In this study, we estimate local axial strain using weighted-least-squares (WLS) regression over a fitting length, Δz [11]. A previous study demonstrated that larger fitting length results in improved strain sensitivity [11], owing to more displacement data points involved in strain estimation within the fitting length, but meanwhile, lower strain axial resolution [18]. In principle, the selected fitting length determines the trade-off between sensitivity and axial resolution. Moreover, the effect of WLS strain estimation on strain sensitivity is dependent on the exact weights (typically inverse OCT SNR) of the data points [11]. However, in practice, the distribution of OCT SNR within the fitting length is non-uniform and, more importantly, is unknown prior to scanning. To simplify the analytical model for QME system sensitivity, we instead incorporate ordinary-least-squares (OLS) strain estimation that is equivalent to WLS in the case of uniform OCT SNR within the fitting length, following the precedent set in previous analysis of strain estimation methods in OCE [11]. Whilst this approach does not account for the relationship between OCT SNR and displacement sensitivity, previous studies have shown that it provides reasonable comparison to experimental results where strain is calculated using WLS [11,18]. Briefly, assuming the displacement measurements are statistically independent and homoscedastic (*i.e.*, the random variable has the same finite variance), within non-overlapping regions, the sample strain sensitivity, $s_{\varepsilon,sample}(z)$, is expressed as [11]:

$$s_{\varepsilon,sample}(z) = \sqrt{\frac{12}{m}}\frac{s_{d,sample}}{\Delta z}, \tag{11}$$

where m is the number of displacement measurements within the fitting length. Substituting Eq. (9) into Eq. (11), $s_{\varepsilon,sample}(z)$ can be further expanded as a function of OCT SNR:

$$s_{\varepsilon,sample}(z) = \sqrt{\frac{12}{m}}\frac{\lambda}{4\pi n_{sample}\Delta z\sqrt{SNR_{OCT,sample}(z) \times N}}. \tag{12}$$

2.1.3.　Stress sensitivity

Combining Eq. (4) with Eq. (10), strain sensitivity in the layer can be obtained:

$$s_{\varepsilon,layer} = \frac{s_{d,layer}}{l_{layer}(\varepsilon_{pre-strain})} = \frac{\lambda}{4\pi n_{layer}l_{layer}(\varepsilon_{pre-strain}) \times \sqrt{SNR_{OCT,layer}N}}. \tag{13}$$

With the strain measured from the layer-sample interface shown in Eq. (4), the layer stress, σ_{layer}, in Eq. (3) can be expanded to:

$$\sigma_{layer} = \frac{E_{layer}(\varepsilon_{pre-strain})}{l_{layer}(\varepsilon_{pre-strain})}d_{layer}. \tag{14}$$

The corresponding stress sensitivity is:

$$\begin{aligned}s_{\sigma,layer} &= E_{layer}(\varepsilon_{pre-strain}) \times s_{\varepsilon,layer} \\ &= \frac{E_{layer}(\varepsilon_{pre-strain}) \times \lambda}{4\pi n_{layer}l_{layer}(\varepsilon_{pre-strain}) \times \sqrt{SNR_{OCT,layer}N}}.\end{aligned} \tag{15}$$

2.1.4.　QME system sensitivity

To simplify the expression for QME system sensitivity, *i.e.*, elasticity sensitivity, we assume that the pre-strain imparted to both the layer and sample are constant over time and, consequently that the layer elasticity, $E_{layer}(\varepsilon_{pre-strain})$, and the layer thickness, $l_{layer}(\varepsilon_{pre-strain})$, are considered as constants. Hence, as shown in Eq. (5), $E_{sample}(z)$ is proportional to the ratio between two random variables d_{layer} and ε_{sample}. Using a first-order Taylor expansion, an approximation to the standard deviation of E_{sample}, elasticity sensitivity, $s_{E,sample}(z)$, can be obtained [36]:

$$\begin{aligned}s_{E,sample}(z) &\approx \frac{E_{layer}(\varepsilon_{pre-strain})}{l_{layer}(\varepsilon_{pre-strain})}\frac{\mu_{d,layer}}{\mu_{\varepsilon,sample}(z)} \\ &\times \sqrt{\left(\frac{s_{d,layer}}{\mu_{d,layer}}\right)^2 + \left(\frac{s_{\varepsilon,sample}(z)}{\mu_{\varepsilon,sample}(z)}\right)^2 - \frac{2Cov(d_{layer},\varepsilon_{sample}(z))}{\mu_{d,layer}\mu_{\varepsilon,sample}(z)}},\end{aligned} \tag{16}$$

Where $\mu_{d,layer}$ represents the mean of d_{layer}, the random variable of layer displacement, and $\mu_{\varepsilon,sample}(z)$ represents the mean of $\varepsilon_{sample}(z)$, the random variable of the depth-resolved local strain in the sample. A similar expression for the approximation to the variance of ratio estimators has also been demonstrated in fluorescence imaging [37]. As d_{layer} and ε_{sample} are obtained from non-overlapping regions, they can be considered to be statistically independent. In this case, the covariance term in Eq. (16) can be set as zero [38]. Substituting Eqs. (10) and (12) into Eq. (16), $s_{E,sample}(z)$, can be expanded as:

$$\begin{aligned}s_{E,sample}(z) &\approx \frac{E_{layer}(\varepsilon_{pre-strain})}{l_{layer}(\varepsilon_{pre-strain})}\frac{\mu_{d,layer}}{\mu_{\varepsilon,sample}(z)} \\ &\times \sqrt{\frac{\frac{1}{SNR_{OCT,layer}N}\left(\frac{\lambda a_{layer}}{4\pi n_{layer}}\right)^2}{\mu_{d,layer}^2} + \frac{\frac{12}{mSNR_{OCT,sample}(z)\times N}\left(\frac{\lambda a_{sample}(z)}{4\pi n_{sample}\Delta z}\right)^2}{\mu_{\varepsilon,sample}^2(z)}},\end{aligned} \tag{17}$$

where a_{layer} and $a_{sample}(z)$ represent noise correction factors used to account for mechanical noise (e.g., jitter from the galvanometers and the ring actuator) in the layer and sample, respectively. The correction factors are determined by the ratio of the experimental displacement sensitivity to the theoretical displacement sensitivity in the layer and the sample, which are defined in Eqs. (9) and (10), respectively. It should be noted, in the case where there is no lateral scanning and the sample is stationary, that both a_{layer} and $a_{sample}(z)$ are assumed to be 1. In summary, the parameters shown in Eq. (17) can be classified into three groups: mechanical parameters $\mu_{d,layer}$, $\mu_{\varepsilon,sample}(z)$, $E_{layer}(\varepsilon_{pre-strain})$, and $l_{layer}(\varepsilon_{pre-strain})$; optical parameters $SNR_{OCT,layer}$ and $SNR_{OCT,sample}(z)$; and signal processing parameters N and Δz.

2.2. Feature sensitivity in QME

In addition to QME system sensitivity, which is measured at a single spatial position in a sample over time, the measured elasticity also could vary spatially throughout a micro-elastogram of a mechanically homogeneous sample due to factors such as OCT speckle [11], phase decorrelation [12,39], surface topology [40] and friction [16,40,41]. Hence, whilst system sensitivity is vital to determine the performance of a QME system, extrapolating from QME system sensitivity to sensitivity in a micro-elastogram will likely overestimate the sensitivity of QME in practical imaging scenarios. To address this issue, we define and measure feature sensitivity as the standard deviation of the measured elasticity over a mechanically homogeneous region in a micro-elastogram of a scattering sample, analogous to how sensitivity was defined in previous OCE studies [6,12]. Note that, as the spatial varying factors are dependent on the specific sample, imaging system and loading conditions, deriving an analytical model of feature sensitivity is outside the scope of this study. Instead, in Section 4.6, we experimentally illustrate the distinction between system sensitivity and feature sensitivity in QME, and we demonstrate a simple method to enhance the feature sensitivity to match system sensitivity by compromising resolution through spatial averaging. For concision, the rest of this manuscript will refer to the terms QME system sensitivity and QME feature sensitivity as simply system sensitivity and feature sensitivity, respectively.

2.3. Resolution in QME

As we consider the trade-off between sensitivity and resolution, in this section, we briefly summarize spatial resolution in QME. Similar to the definition of sensitivity in this study, a previous study by our group showed that spatial resolution in compression OCE can be considered as both a system and a feature parameter, namely system resolution and feature resolution [18]. System resolution is defined as a combination of the OCT and signal processing resolution as is independent of the sample. Feature resolution is defined as the measured resolution of features in a micro-elastogram using the step response in strain or elasticity across a feature boundary. Importantly, feature resolution was shown to be dependent on factors such as mechanical contrast and feature size. System resolution is described as the FWHM of the resultant point-spread function (PSF) of the OCT PSF, $\text{PSF}_{OCT}(x, z)$ [42], convolved with the OLS PSF, $\text{PSF}_{LSR}(z)$, which is an inverted parabola with FWHM of $\Delta z/\sqrt{2}$ [18]:

$$\text{PSF}_{system}(x, z) = \text{PSF}_{OCT}(x, z) \otimes \text{PSF}_{LSR}(z). \tag{18}$$

Additionally, since in this study we incorporate spatial averaging to observe the effect of trading off feature sensitivity, system resolution and feature resolution, the contribution of spatial averaging to QME system resolution can be extended as:

$$\text{PSF}_{system}(x, z) = \text{PSF}_{OCT}(x, z) \otimes \text{PSF}_{LSR}(z) \otimes \text{PSF}_{Avg}(x, z). \tag{19}$$

The system resolution can thus be estimated analytically by measuring the FWHM of the resultant PSF_{system}. Note that the system resolution was measured using Eq. (18) in Sections 4.1 as no extra spatial averaging is incorporated in the signal processing. By contrast, the system resolution in Section 4.6 that demonstrates the impact of spatial averaging on feature sensitivity and feature resolution in QME was measured using Eq. (19).

2.4. Accuracy in QME

Given sufficiently high OCT SNR from both the layer-sample interface and the sample, it is generally assumed that the corresponding displacement and strain are unbiased, *i.e.*, the expected value of the elasticity random variable corresponds to the true sample elasticity [11,33]. However, due to the boundary effects existing in mechanical deformation, friction impedes the lateral

expansion of the sample and the layer, which affects the accuracy of elasticity measurements. Lubricant is a common solution to mitigate the friction at the layer-window and layer-sample interfaces [40]. In addition, it has been suggested that the thickness of the compliant layers is related to the friction at the boundaries [41,43], which could also affect the accuracy in elasticity estimation. Thus, apart from the analysis of sensitivity, we demonstrate the impact of friction and layer thickness on accuracy in Sections 4.3 and 4.4, respectively.

3. Method

3.1. Phase-sensitive QME system setup and procedure

A schematic of the QME experimental setup is shown in Fig. 1. The OCT system used in this study is a fiber-based spectral-domain OCT system (Telesto 220; Thorlabs Inc., USA). The superluminescent diode employed as a light source has a central wavelength of 1300 nm and a spectral bandwidth of 170 nm. The measured OCT axial resolution is 4.8 μm (FWHM in air). The scan lens (LSM03; Thorlabs Inc.) has a measured lateral resolution (FWHM in air) of 7.2 μm. The location of the OCT focus position was controlled by an OCT focus block (MGZ30; Thorlabs Inc., USA) which has 30 mm of travel range with fine adjustment of 225 μm/rev. The mechanical loading method has been detailed previously [2,3]. Briefly, a 75 mm diameter imaging window (IW in Fig. 1) (Edmund Optics Inc., USA), fixed with wax to a ring actuator (RA in Fig. 1) (Piezomechanik GmbH, Germany) with an internal aperture of 65 mm, was placed below the scan lens to enable imaging and actuation in the layer and the sample. The system was configured in common-path [2,23], where the interface between the imaging window and the layer acted as the reference reflector. Lubricant (AK50 silicone oil; Wacker, Germany) was applied to reduce the friction at the window-layer interface and the layer-sample interface. The sample (S in Fig. 1) was placed between a compliant layer and a translation stage which was used to provide a pre-strain of 20% imparted to the layer-sample system in experiment.

To investigate the effect of temporal averaging on system sensitivity and accuracy in Sections 4.1, 4.2 and 4.3, a total of 10,000 complex OCT B-scan pairs (unloaded-loaded) were acquired at the same y-position from a homogenous silicone phantom. Each B-scan comprised 1,000 A-scans per B-scan over a 2 mm lateral range (2 μm per voxel). Subsequently, the (complex) phase difference between each pair of unloaded and loaded complex OCT B-scans was calculated using the Kasai phase estimator [44]. Each block of N (up to 50) phase difference B-scans was averaged to produce each output B-scan. The first 200 averaged B-scans were then used to calculate displacement, strain, elasticity and sensitivity. System sensitivity was then calculated from the standard deviation of the 200 elasticity measurements. It should be noted that, in Section 4.1, 4.2 and 4.3, five measurements of QME system sensitivity measured from five bright pixels, which have the same OCT SNR of ~35 dB at the same depth, were used to produce the mean and standard deviation of system sensitivity to account for the noise of measurements. Additionally, the data used for the results shown in Section 4.4 and Section 4.5 were acquired and processed in the same way, except on 2000 B-scan pairs were acquired, and only $N = 10$ B-scan pairs were averaged for each output B-scan. Similarly, for the results shown in Section 4.6, 10,000 B-scan pairs at the same y-position were acquired of a structured inclusion phantom, each comprising 1,000 A-scans per B-scan over a 4 mm lateral range (4 μm per voxel), with $N = 50$ B-scan pairs averaged for each output B-scan. All analysis of the data in Sections 4.4, 4.5 and 4.6 were performed on 200 output B-scans.

The axial displacement at each pixel is calculated from the phase difference between an unloaded-loaded B-scan pair acquired at the same spatial location. The local axial strain is calculated as the slope of the axial displacement with depth using WLS regression over a 1-D fitting length (Δz), typically 100 μm (~30 pixels). To improve feature sensitivity, we incorporate spatial averaging in the signal processing at the very last step, by convolving the micro-elastogram with a smoothing filter. Gaussian smoothing filters have been commonly applied to improve the
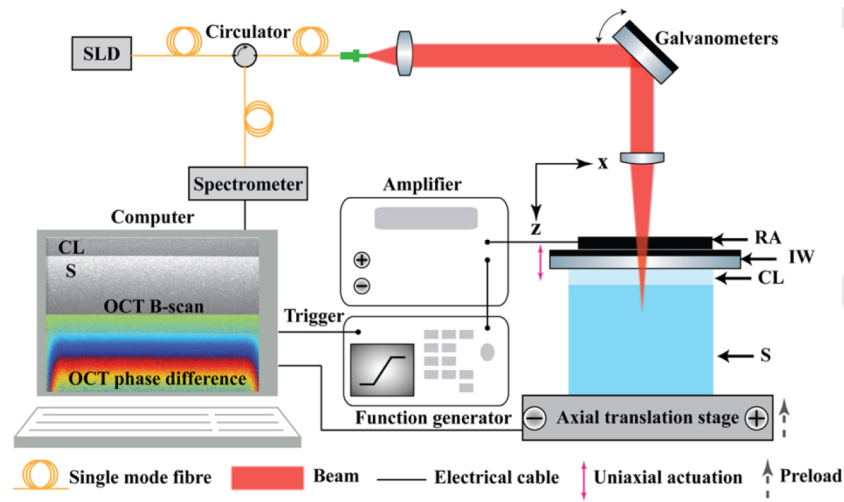
Fig. 1. QME experimental setup comprising a phase-sensitive OCT system, a compressive loading setup and signal processing. SLD: superluminescent diode, RA: ring actuator, IW: imaging window, CL: compliant layer, S: sample.

image quality in OCE, at the cost of resolution [9–11,45]. In this paper, we implement Gaussian smoothing to analyze the trade-off between feature sensitivity, system resolution and feature resolution by varying the FWHM of the 2-D isotropic Gaussian kernel. The stress-strain curves of the compliant layers were pre-characterized using a uniaxial compression testing apparatus described previously [28].

3.2. Tissue-mimicking phantom and compliant layer fabrication

To investigate QME sensitivity and accuracy, two structured tissue-mimicking phantoms and three compliant layers with different thicknesses were fabricated. Phantom 1, made from Elastosil P7676 (Wacker, Germany), is a 3 mm thick cylinder with a diameter of 10 mm and was designed to be optically and mechanically homogeneous. The Young's modulus of Phantom 1 at a pre-strain of 20% is 18.7 ± 1.2 kPa measured from uniaxial compression tests on a silicone cylinder with an aspect ratio of 1, which is consistent to the measured values reported in our recent publications [10,18]. To provide optical scattering, TiO_2 particles with a mean diameter of 1 μm and a refractive index of 2.3 were evenly mixed into the silicone at a concentration of 2 mg/ml. Phantom 2 was fabricated using the same bulk materials as Phantom 1, but additionally contained a stiff inclusion (327 ± 18.4 kPa at a pre-strain of 20%), which was embedded ∼ 375 μm below the surface. To minimize the out-of-plane (y) motion in a B-scan [46], which would result in inaccurate axial strain estimation in QME, the inclusion was manufactured to be a strip which has the dimension of 0.56 mm × 8 mm × 0.53 mm ($x \times y \times z$). The inclusion was fabricated from Elastosil RT601 and AK50 Silicone oil (Wacker, Germany). The bulk region of Phantom 2 contains TiO_2 particles at a concentration of 2 mg/ml, whilst the inclusion contains TiO_2 particles at a concentration of 10 mg/ml. To investigate the impact of layer aspect ratio on system accuracy, three transparent layers with a diameter of 10 mm were fabricated from Elastosil P7676, with thicknesses of 150 μm, 420 μm, and 925 μm, respectively. The specific layer thicknesses were achieved using a spacer made from two 50 mm × 50 mm × 5 mm non-adhesive Acrylic plates and a stack of 50 μm thick tape.

4. Results

4.1. *Comparison of QME system sensitivity between theory and experiment*
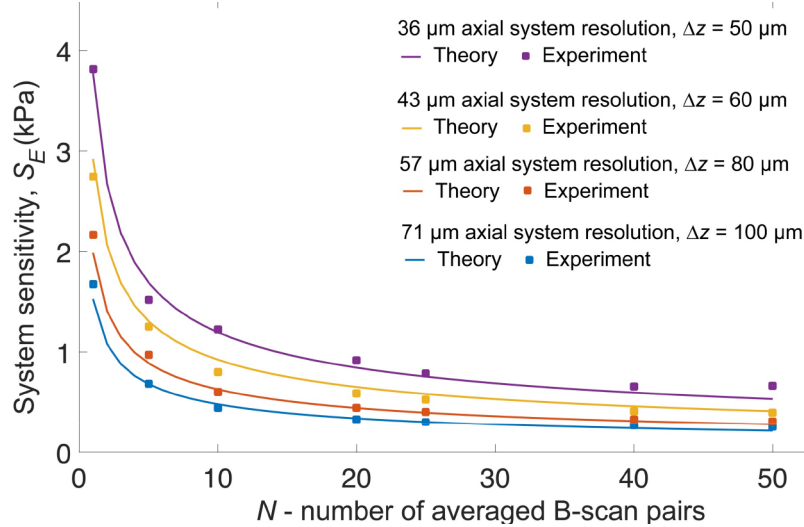

Fig. 2. Comparison between the theoretical (Eq. (17)) and experimental QME system sensitivity as a function of temporal averaging at axial system resolutions of 36 μm (purple), 43 μm (yellow), 57 μm (orange), and 71 μm (blue). The theoretical measurements are denoted by solid lines and the experimental measurements are denoted by solid squares.

In this section, we validate the analytical model of QME system sensitivity (Eq. (17)) through comparison with experimental scans of homogeneous Phantom 1. An unlubricated layer with a thickness of 420 μm was placed on top of the sample to measure surface stress. A pre-strain of 20% was applied on the layer-sample system to ensure uniform contact, resulting in a pre-strained layer thickness (l_{layer}) of 378.2 μm, measured from the OCT image, and a tangent modulus of the layer (E_{layer}) of 14.2 kPa, measured from the uniaxial compression tests. To determine the noise correction factors in the experimental setup, we measured the theoretical and experimental displacement sensitivities using the first 200 B-scans without temporal averaging. Five spatial locations with an OCT SNR of ~35 dB at the same depth were chosen at the layer-sample interface, and $s_{d,layer} = 3.6$ nm was calculated as the spatial average of the standard deviations of layer displacement measurements at each location. Similarly, at the same x-positions, five locations with an OCT SNR of ~35 dB were chosen at the same depth in the sample, and $s_{d,sample} = 3.6$ nm was calculated as the average of the standard deviations of sample displacement measurements at each location. Using Eqs. (9) and (10), the corresponding theoretical displacement sensitivity in the layer and sample at the SNR of 35 dB is 1.5 nm. Using Eq. (17) and solving for the noise correction factors gives $a_{layer} = 2.4$, and $a_{sample} = 2.3$, for the layer and sample, respectively. Analogous to experimental displacement senstivity, to best compare between theory and experiment, $\mu_{d,layer} = 94.5$ nm calculated as the spatial average of means of layer displacement from the first 200 B-scans at each location of the layer, and $\mu_{\varepsilon,sample} = 0.038$ calculated as the spatial average of means of sample strain at each location of the sample, were substituted in the theoretical model (Eq. (17)) to replace $\mu_{d,layer}$ and $\mu_{\varepsilon,sample}$, respectively, which used to generate the theoretical results in Section 4.1.

Figure 2 shows the comparison between theoretical and experimental system sensitivity with temporal averaging (N) varied from 1 to 50 B-scan pairs, at strain fitting lengths (Δz) of 50 μm, 60 μm, 80 μm and 100 μm, corresponding to axial system resolutions of 36 μm, 43 μm, 57 μm and

71 µm, respectively (FWHM measured using Eq. (18)). For different axial system resolutions, the plots of theoretical QME system sensitivity agree well with the experimental results. Whilst system sensitivities improve to some extents as the temporal averaging increases from 1 to 50, the rate of improvement drops rapidly in both theory and experiment for all the plots after 10 B-scan pairs. As expected, the larger Δz leads to better elasticity sensitivity but worse axial system resolution. Without temporal averaging ($N = 1$), the QME system sensitivity is ~ 1.5 kPa with $\Delta z = 100$ µm, which is ~ 2.5 times better than that with $\Delta z = 50$ µm. As a trade-off, the corresponding axial system resolution is twice as large. However, by performing temporal averaging more than 6 B-scan pairs, the QME system sensitivity with $\Delta z = 50$ µm starts to become better than with $\Delta z = 100$ µm and $N = 1$. Meanwhile, the axial system resolution can still be maintained at 36 µm with $\Delta z = 50$ µm. This suggests QME system sensitivity and resolution can be improved simultaneously by trading off time for averaging.

4.2. Mechanical deformation: effect of friction on QME system sensitivity

In this section, we examine the system sensitivity using the homogeneous Phantom 1 both with and without lubrication. For lubricated measurements, a drop of silicone oil (~ 50 µl) was added to both the window-layer and layer-sample interfaces to reduce surface friction. Figures 3(a)–3(d) show plots of experimental layer strain sensitivity, layer stress sensitivity, sample strain sensitivity and system sensitivity (mean $\pm$ standard deviation) as a function of temporal averaging overlaid with the corresponding theoretical sensitivities using Eq. (17), for both the unlubricated and lubricated cases. The squares and error bars represent the mean and standard deviation of sensitivities measured from five bright pixels, as described in Section 3.1.

As expected, increasing temporal averaging from 1 to 50, both theoretical and experimental system sensitivities of strain, stress and elasticity are shown to be improved for both lubrication cases. For all four sensitivity plots shown in Figs. 3(a)–3(d), the sensitivity of the lubricated system is always poorer than the unlubricated system. In experiment, we observed that the layer experienced more lateral expansion in the measurements with lubrication, hence, smaller l_{layer}. From Eq. (13), the layer strain sensitivity is inversely proportional to the layer thickness at a given pre-strain. The smaller layer thickness at a given pre-strain results in worse layer strain sensitivity, which matches the results seen in Fig. 3(a). In Fig. 3(b), we show that the difference in the layer strain sensitivity between lubricated and unlubricated conditions is amplified in the measured layer stress sensitivity. Under the same 20% pre-strain imparted to the layer-sample system, lubrication results in a greater measured pre-strain in the layer ($\sim 26\%$) than the unlubricated layer pre-strain ($\sim 8\%$), and hence a larger E_{layer} due to the nonlinear stress-strain curve of the layer. From Eq. (15), this leads to a worse measured layer stress sensitivity than under unlubricated conditions. From Fig. 3(c), and comparing to Fig. 3(a), the sample strain sensitivity is poorer than the layer strain sensitivity in both the unlubricated and lubricated cases. This is likely due to the combination of the strain-induced phase decorrelation noise resulting from the higher strain in the layer and sample, as shown in Figs. 4(a) and 4(c), and the translation-induced phase decorrelation noise increasing with depth [12]. Additionally, in Fig. 3(c) the experimental sample strain sensitivity without lubrication is close to that measured with lubrication when a temporal averaging less than 5 B-scan pairs is performed. Beyond that, in experiment the difference between these two increases. As expected, in Fig. 3(d), the QME system sensitivity in lubricated measurements is consistently lower than that in unlubricated measurements, both in theory and experiment.

Additionally, for all the results shown in Fig. 3, the lubricated experimental sensitivities are worse than the theoretical sensitivities. As the temporal averaging increases, the discrepancy between the experimental results and the theoretical predictions increases and appears to converge to a constant offset. This suggests a time-dependent effect that degrades the QME system sensitivity in experiment. This effect is possibly due to a temporal variation in the lubrication at
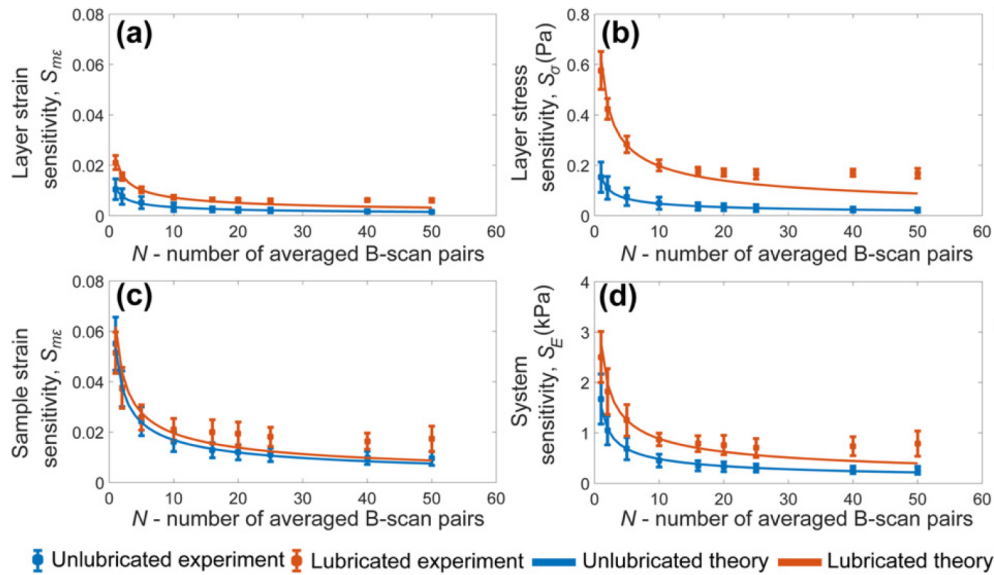
Fig. 3. The effect of lubrication on QME system sensitivity as a function of temporal averaging (N) in both theory (solid lines) and experiment (solid squares). (a) Layer strain sensitivity; (b) layer stress sensitivity; (c) sample strain sensitivity; (d) QME system sensitivity. All experimental results are shown as mean ± standard deviation.

the boundaries of the layer, which was not considered in the theoretical predictions (Eq. (17)) in this study. This temporal effect is further discussed Section 5. Despite this, it should be noted that a QME system sensitivity of 0.7 kPa is still achievable with the 25 B-scan pair averaging in experiment.

4.3. Mechanical deformation: effect of friction on QME accuracy

In this section, we examine the changes in QME accuracy using the homogeneous Phantom 1 both with and without lubrication. Figure 4 demonstrates that the mean of measured strain, stress and elasticity under different lubrication conditions are independent of temporal averaging. In Fig. 4(a), the magnitude of the strain (Fig. 4(a), layer strain; Fig. 4(c), sample strain), layer stress (Fig. 4(b)), and the resulting elasticity (Fig. 4(c)) are higher in the lubricated system than in the unlubricated system. Under the same pre-strain and stroke of the ring actuator, for the incompressible layer and sample, lubrication enables more lateral expansion during mechanical deformation, resulting in higher measured strain in both materials. Analogous to layer stress sensitivity in Fig. 3(b), the difference in layer stress between lubricated and unlubricated measurements is also increased in Fig. 4(b).

In Fig. 4(d), we demonstrate the comparison of elasticity between unlubricated and lubricated QME measurements, overlaid with the Young's modulus of the same material measured from uniaxial compression tests at the same pre-strain. The mean elasticity measured using QME in the lubricated case is ~17.1 kPa, within 9% of the compression tests, whilst the unlubricated measurement was ~9.7 kPa, ~48% difference compared to the compression tests. It is also worth noting that both the unlubricated and lubricated measurements underestimated the true elasticity. The underestimation in both cases is likely due to the difference of boundary conditions of the layer between QME loading setup and uniaxial compression setup, which is further explained in Section 5. These results suggest that lubrication does not fully remove the effects of friction from elasticity measurements.
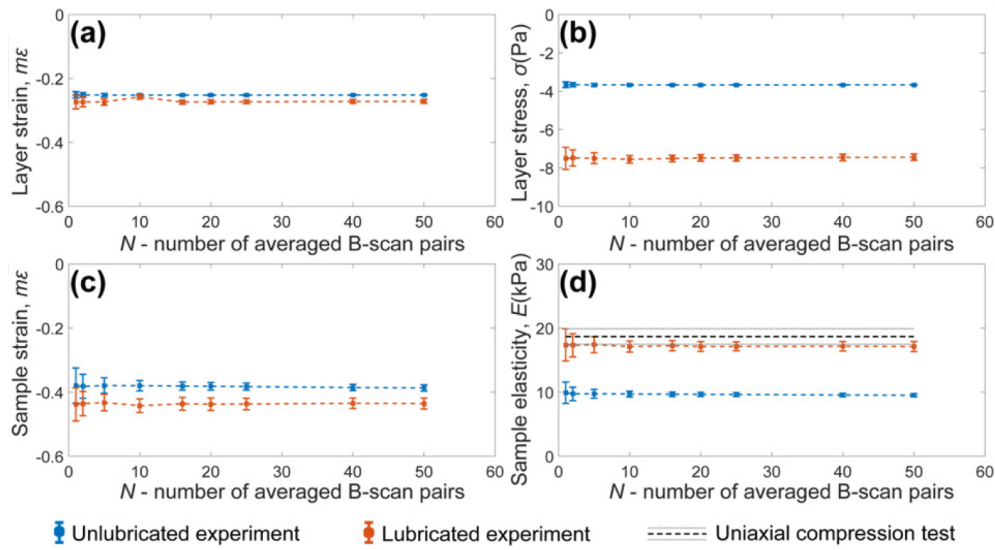
Fig. 4. The system accuracy as a function of temporal averaging (*N*) with (orange) and without lubrication (blue). (a) Layer strain; (b) layer stress; (c) sample strain; (d) the comparison of elasticity measurements in QME under different lubrication to the uniaxial compression tests (grey double dashed line). All experimental results are shown as mean ± standard deviation.

4.4. Mechanical deformation: effect of layer thickness on system accuracy

In this section, we investigate the effect of layer thickness on system accuracy. Layers with thicknesses of 150 μm, 420 μm and 925 μm, respectively, were lubricated and placed on Phantom 1. At a pre-strain of 20% imparted to the three different layer-sample systems, the pre-strain measured in the sample was ~20%. In this experiment, 50 elasticity measurements were first averaged over a lateral range of 100 μm at each depth in a single B-scan of elasticity. Subsequently, the mean elasticity at each depth was calculated from 200 temporally averaged B-scans of elasticity at the same *y*-position. To ensure consistent QME measurements, the OCT beam focus was set at the layer-sample interface in each case. As the position of the layer-sample interface varies for the different layer thicknesses, we plot the elasticity as an offset from the layer-sample interface (labelled as "effective imaging depth"), until the OCT signal reached the noise floor. This resulted in a different effective imaging depth, *i.e.*, the thinner the layer the greater effective imaging depth. The results are shown in Fig. 5. Analogous to Fig. 4(d), the QME measurements are also overlaid with the uniaxial compression tests to examine the accuracy.

In Fig. 5, the elasticity measured with a 150 μm thick layer marked in solid blue has the largest effective imaging depth; approximately three times that of the 925 μm thick layer, owing to the layer-sample interface being closest to the common-path reference reflector. In comparison to the uniaxial compression tests, the 150 μm thick layer consistently underestimates the true elasticity and this effect increases with depth. By contrast, the 420 μm thick layer overestimates elasticity above the effective imaging depth of ~0.32 mm. Below the depth of ~0.32 mm, the elasticity accuracy, using the 420 μm thick layer, increases with depth and reaches a steady state, which is similar to the trend of the 150 μm thick layer. The similar trend of the decreased elasticity with the depth is likely attributed to the surface friction which restricts sample deformation, *i.e.*, less sample strain, closer to the layer-sample interface, but has less effect at deeper regions. However, the underestimation of elasticity using the 150 μm thick layer is due to the underestimation of layer stress. In experiment, at the same pre-strain of 20% imparted to the layer-sample system,
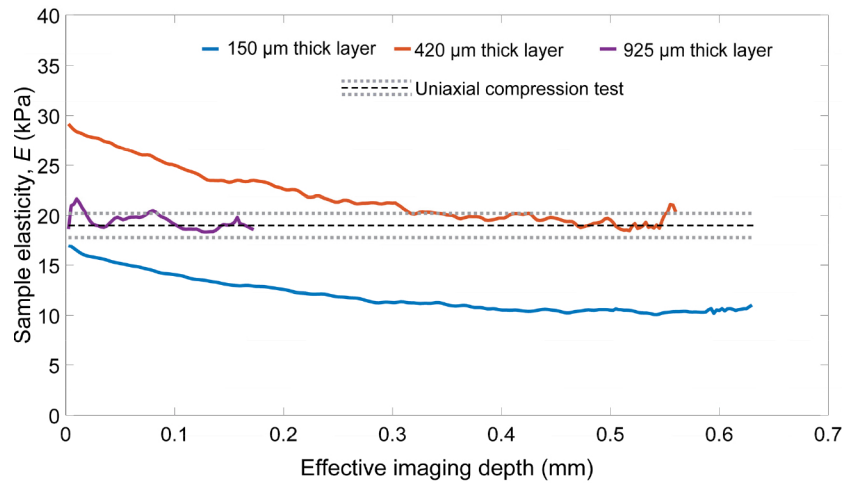
Fig. 5. The QME system accuracy with effective imaging depth using layers with thicknesses of 150 μm (blue), 420 μm (orange) and 925 μm (purple), compared to the uniaxial compression tests, where the mean of true elasticity of Phantom 1 is denoted by a black dashed line and the standard deviation is denoted by a grey double dashed line.

the resulting pre-strain measured in the 150 μm thick layer (~5%) is less than both the 420 μm thick layer (~30%) and the 925 μm thick layer (~27%). The smallest layer pre-strain measured in the 150 μm thick layer leads to the underestimation of layer stress and, hence, sample elasticity. By contrast, the 925 μm thick layer provides the greatest accuracy but has a limited effective imaging depth as a trade-off. It was suggested in the mechanics of uniaxial compression that the surface friction increases as the thickness of specimen decreases [41,43]. Hence, it is expected that minimum friction at the boundaries of the thickest layer (*i.e.*, the 925 μm thick layer) enables accurate strain and stress to be measured in the layer, leading to the greatest accuracy of elasticity measurements.

4.5. OCT: effect of the focus position on QME system sensitivity

Equation (17) shows that QME system sensitivity is also dependent on OCT SNR, which can be varied by changing the focus position of the objective lens in the OCT system. To avoid the temporal effect caused by lubricant on QME system sensitivity, as described in Section 4.2, the layer-sample interface was not lubricated in this experiment. In Fig. 6 we present experimental results, from Phantom 1 with the 420 μm thick layer, of the OCT SNR and QME system sensitivity as a function of focus position of the OCT beam. The double dashed lines marked in OCT images represent the depth of focus (×2 Rayleigh range (Z_R)), which for the OCT system used has a theoretical value of ~ 180 μm in air. Five focus positions were chosen, each focus position setting is described as a function of Z_R in Figs. 6(a)–6(e). The upper limit of the first focus position is above the common path reference, and not shown in Fig. 6(a). 10 B-scan pairs (unloaded-loaded) from the same spatial location were averaged to produce the B-scan images in Figs. 6(a)–6(e). A further 50 A-scans (100 μm) were averaged to produce the plots shown in Fig. 6(f). The corresponding QME system sensitivity measurements as a function of depth (measured from the center A-scan across the 200 B-scans) are presented in Fig. 6(g). Similar to Section 4.4, the effective imaging depth was also used in Figs. 6(f) and 6(g) by offsetting the depth from the layer-sample interface to a point above the noise floor of QME measurements. Additionally, to better present the trend of the QME system sensitivity with depth at varying OCT focus positions, we overlaid the raw depth-dependent QME system sensitivity, marked in semi-transparent dashed

lines, with smoothed QME system sensitivity plots using a second order Savitzky-Golay filter, with length 163 pixels (∼554 μm), marked in solid lines.
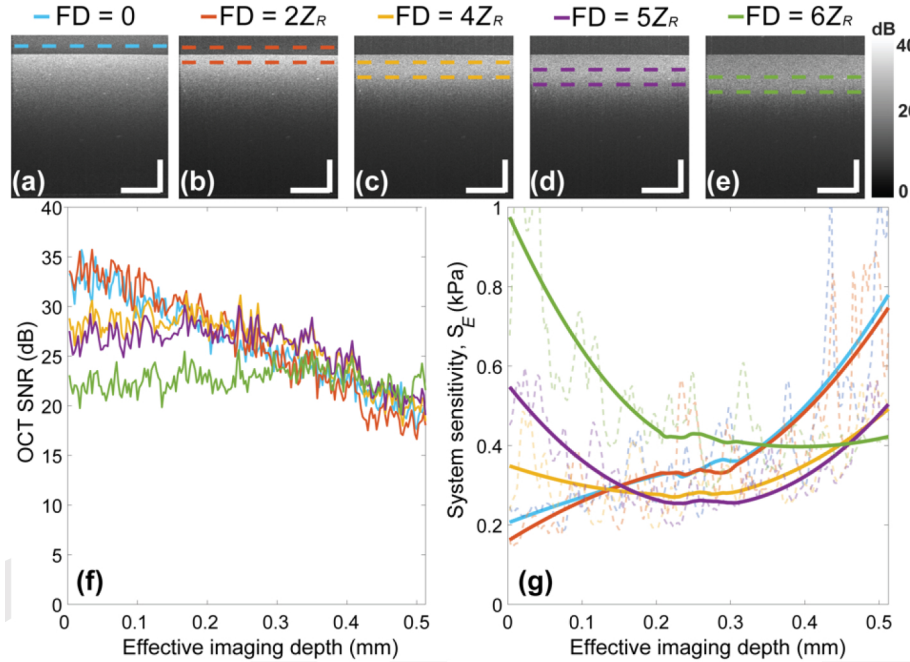

Fig. 6. The impact of focus depth (FD) on QME system sensitivity as a function of imaging depth, corresponding to five focus depths relative to the imaging reference, as shown in (a)-(e). (f) The corresponding OCT SNR with the imaging depth at five different focus depths; (g) the QME system sensitivity with the imaging depth at five different focus depths. The focus depth is represented as a function of the Rayleigh range (Z_R). The depth of focus ($2Z_R$) is marked by double dashed lines. The filtered depth-resolved QME system sensitivity measurements (solid lines) using a second order Savitzky-Golay filter are overlaid with the raw QME system sensitivity measurements (semi-transparent dashed lines). Scale bars represent 500 μm.

Figure 6(f) shows, by setting the focus position below the interface, that the peak of the OCT SNR was located within the sample, to the point that the OCT SNR-depth profile became flattened at a focus position of $6Z_R$ (green), owing to the contributions of OCT focus position and attenuation in the sample. Specifically, lowering the focus position to $6Z_R$ reduces the reference power in common-path configuration, which reduces the overall OCT SNR, but the depth range around this focus position has an increased OCT SNR. These two combinational effects cancel out the sample attenuation, leading to low OCT SNR everywhere in the green plot. Figure 6(g) shows, when the focus position was set at the reference (cyan) and at a position of $2Z_R$ from the reference (orange), respectively, that the estimated QME system sensitivity consistently degrades with depth. By contrast, with the focus at $5Z_R$, the estimated QME system sensitivity at regions close to the sample surface is inferior to shallower focus position. However, the estimated QME system sensitivity improves gradually with depth and reaches a peak that is even better than the best sensitivity measurements achieved by the shallower focus positions. In contrast, for the deepest focus position (FD = $6Z_R$ (green)), the QME system sensitivity starts very poor, but improves with depth before reaching a value of ∼0.4 kPa at depths greater than 0.22 mm. Beyond the depth of 0.35 mm, the corresponding QME system sensitivity starts to become better than that measured with both FD = 0 and FD = $2Z_R$. After the depth range between 0.46 mm and 0.51

mm, the estimated QME system sensitivity is superior to that measured with both $FD = 4Z_R$ and $FD = 5Z_R$, respectively.

4.6. Signal processing: trade-off between feature sensitivity, system resolution and feature resolution

In this section, we further demonstrate the trade-off between feature sensitivity and feature resolution as a function of system resolution in Fig. 7, from an experimental scan of an inclusion phantom (Phantom 2). The experimental OCT B-scan and corresponding micro-elastogram are shown in Figs. 7(a) and 7(b), respectively. The strain fitting length (Δz) was set to 100 µm. We convolved the micro-elastogram (Fig. 7(b)) with an isotropic spatial Gaussian smoothing kernel with FWHM varying from 0 µm to 80 µm. A kernel of 80 µm FWHM degrades the axial system resolution from 71 µm to 108 µm and the lateral system resolution from 7.2 µm to 80 µm, with both determined from Eq. (19) in Section 2.3. The black dotted line in Fig. 7(b) indicates the locations where feature resolution was measured from the step response of elasticity across the stiff inclusion in the micro-elastogram, in both axial and lateral directions. The corresponding axial and lateral feature resolution, as a function of axial system resolution and lateral system resolution, measured from experiments are shown in Figs. 7(e) and 7(f), respectively. The feature sensitivities, plotted in Figs. 7(g) and 7(h), were measured as the standard deviation of the elasticity values within a 280 µm × 25 µm ($x \times z$, ~70 × 10 pixels) rectangular window, marked by the red boxes in Figs. 7(c) and 7(d). The QME system sensitivity was measured as the standard deviation of elasticity values at a point (~1.6 kPa), over the 200 B-scans of elasticity at the same y-position, within this window.

Figure 7(g) shows that, as the axial system resolution decreases from 71 µm to 95 µm, the feature sensitivity marked in blue dotted line is improved from 9.5 kPa to 1.6 kPa, matching the system sensitivity. As a trade-off, the corresponding axial feature resolution degrades from 107 µm to 125 µm (Fig. 7(e)). Similarly, Fig. 7(h) shows that the lateral system resolution needs to be compromised from 7.2 µm to 60 µm for the improvement of feature sensitivity to match system sensitivity at 1.6 kPa, at the expense of degrading lateral feature resolution from 90 µm to 140 µm (Fig. 7(f)). After the matching point, the increased kernel size of Gaussian smoothing keeps improving the feature sensitivity past the QME system sensitivity. This is because as the amount of spatial averaging increases, the entire image converges to a single value (*i.e.*, a feature sensitivity of zero).
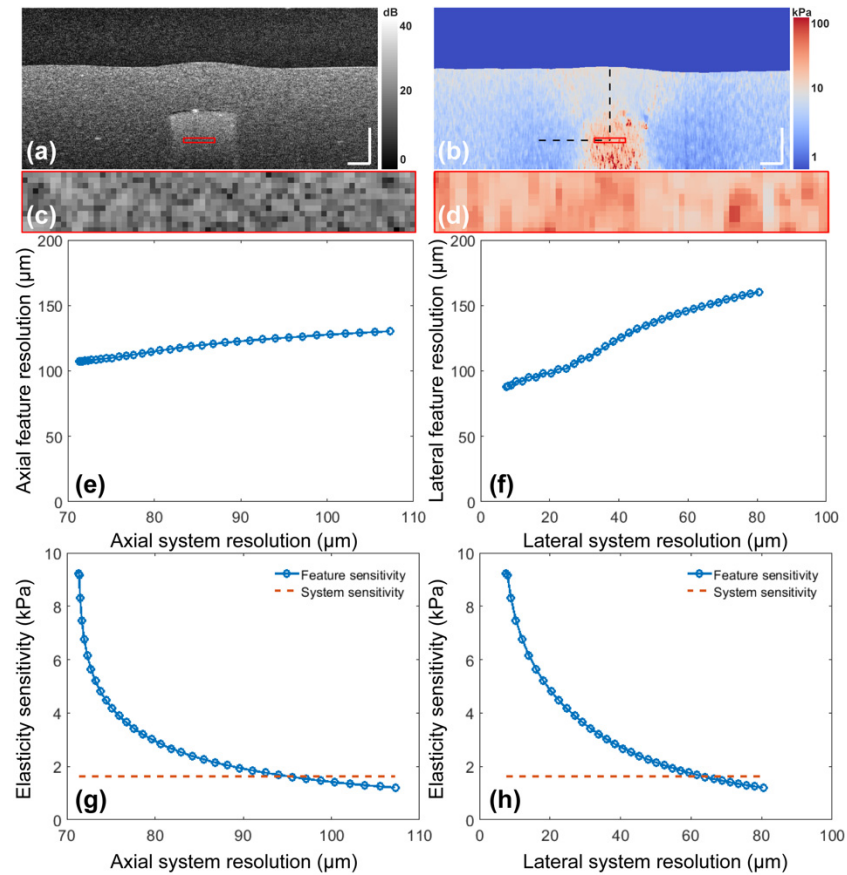
Fig. 7. The trade-off between QME feature sensitivity, feature resolution and system resolution. (a) The cross-sectional OCT B-scan and the corresponding elasticity micro-elastogram are shown in (a) and (b), respectively. The zoomed regions (280 µm × 25 µm, corresponding to 70 × 10 pixels) shown in (c) and (d) represent the window for feature sensitivity measurement. (e) axial feature resolution versus axial system resolution; (f) lateral feature resolution versus lateral system resolution; (g) feature sensitivity (blue square dotted line) versus axial system resolution overlaid with system sensitivity (orange dashed line); (h) feature sensitivity versus lateral system resolution overlaid with system sensitivity. Scale bars represent 200 µm.

5.　Discussion

In this paper, we have presented the first study of sensitivity in QME that combines the mechanical deformation, OCT system and signal processing. We classify sensitivity as system sensitivity, *i.e.*, sensitivity determined by the imaging system alone and feature sensitivity, *i.e.*, sensitivity determined by both the imaging system and the sample. To support this framework, for the first time, we have demonstrated an analytical model for system sensitivity, validated by close correspondence with experimental results. Using this framework, we investigated the effect of friction, OCT focus depth, strain fitting length of WLS regression and temporal averaging on system sensitivity. Furthermore, we have demonstrated that friction introduces a systematic bias to the measured elasticity by comparing QME measurements to uniaxial compression tests. Here, we demonstrated that lubrication improves the accuracy at the cost of sensitivity. Separately, based on a similar framework proposed for the analysis of resolution in OCE [18], we have extended the method for measuring QME resolution and further analyzed the trade-off between sensitivity and resolution from the effect of signal processing. To optimize the imaging parameters, we have demonstrated that, by reducing feature resolution, the feature sensitivity can be improved to match system sensitivity which has not been considered in previous QME studies. Such a framework enables us to identify suitable applications by evaluating the technique with given imaging metrics, and to optimize QME image quality for a given application.

In Section 4.3, the results suggest that lubricant can significantly improve the measurement accuracy, whilst a discrepancy between the lubricated QME measurement and the uniaxial compression tests which we considered to be the "Ground truth" still exists, as shown in Fig. 4(d). This is likely due to the difference in boundary conditions of the compliant layer between the two compression setups. To address this, in future studies, an OCT system could be integrated into the uniaxial compression test apparatus to ensure the same boundary conditions exist in both measurements. Although our results suggest that the measurement accuracy can be improved using lubricant, as a trade-off, we observed a temporal effect (*i.e.*, the exudation of lubricant at the layer boundaries) that degrades sensitivity, as shown in Fig. 3. This may limit the effectiveness of temporal averaging in some applications with relatively long acquisition times, such as imaging cells and biomaterials *in vitro* [5–7]. Similar effects were also found in another study for imaging viscoelasticity [47], where creep strain depends on the steady-state loss of the sample volume. In that study, Wijesinghe *et al.* reported that the measured creep strain is linked to the amount of lubrication, which introduces a discrepancy between the measured creep strain and the true viscoelastic behavior. Using more viscous lubricant could reduce such temporal effects to improve sensitivity. However, as a trade-off, increased static friction may degrade the accuracy. To optimize QME performance, the impact of lubricant viscosity on the sensitivity and accuracy needs to be further investigated.

Additionally, it should be noted that the results shown in Figs. 3 and 4 were obtained using a homogeneous silicone phantom with a bulk Young's modulus of 18.7 ± 1.2 kPa at 20% bulk strain. Previous QME studies have briefly assessed the repeatability of QME measurements with varying sample stiffness [2,28]. These studies show the precision worsening as the sample elasticity increases. This is consistent with Eq. (17), which suggests that QME system sensitivity is inversely proportional to the sample strain and proportional to layer pre-strain tangent modulus, which is in turn proportional to the sample stiffness. *i.e.*, QME system sensitivity is expected to worsen with increasing sample elasticity. We also observe this effect in Figs. 3 and 4. Specifically, due to the nonlinear elastic behavior of the silicone layer, the increased measured layer pre-strain in the lubrication case results in the greater tangent modulus of the layer and, hence, greater sample elasticity, as suggested in Eq. (5). For a similar reason, the noise in the layer strain measurements is amplified in the layer stress measurements due to the increased tangent modulus of the layer in response to a greater layer pre-strain in the lubricated case. Thus, in parallel, the lubrication of the layer inevitably degrades system sensitivity, as suggested in Eq. (17). In a future

study, one could assess the dependence of system sensitivity on the absolute value of elasticity for samples with varying stiffness. However, it can be expected both system sensitivity and elasticity measurements could vary for different layer-sample systems, which makes it difficult to compare system sensitivity in different cases. The coefficient of variation (the ratio between system sensitivity and mean), which has been used in the system characterization of dynamic OCE [48,49], could provide different metric for characterizing QME.

In the results shown in Fig. 5 the elasticity measured from QME varies significantly with depth, even though the sample is of homogeneous mechanical properties. We attribute this difference to the effects of surface friction, which restricts deformation of the layer and sample at regions close to the surface [16,40,41]. In previous QME publications, this effect appeared to be less pronounced than in Fig. 5. This could be attributed to two main reasons. Firstly, the layers used in previous publications are slightly thicker than that of this study [2,3]. The reported layer thickness ranges from 550 μm to 650 μm and, hence, the measurements could be less affected by the friction. Additionally, in most of the previous OCE or QME studies, measurements were usually presented in *en face* micro-elastograms. As the effect of friction on sample strain is depth-dependent, the measured strain or elasticity appears more uniform in an *en face* micro-elastogram than a B-scan. In addition, as the imaging field of QME is typically several millimeters from the tissue boundary, future work could focus on a method to measure and analyze the friction. This would elucidate the inherent limit on sensitivity and the accuracy in QME, or any of other contact-based imaging modality, imposed by friction. Frictional force at slip boundaries can be inferred by shear strain, which was demonstrated in slip ultrasound elastography by Chakraborty *et al.* [50]. Shear strain at sample boundaries in compression OCE, which could be measured from the local axial and lateral displacement using cross-correlation coefficients by digitally shifting complex OCT scans [45,51–53], could provide a useful indicator to characterize the mobility of biological tissue such as tumors for clinical applications. Additionally, it is expected that the bulk refractive index should not directly affect QME accuracy which is essentially determined by strain accuracy. Strain is a unitless quantity, the spatial derivative of displacement, and does not directly depend on the refractive index, as suggested in Eqs. (2) and (4).

The results shown in Fig. 6 demonstrates the tradeoff between system sensitivity and imaging depth. Specifically, by focusing the OCT beam on a deeper region, the system sensitivity at a shallow region which is out of the focus can be traded off for better system sensitivity at the deeper, focused region. Whilst we present the plots of OCT SNR and system sensitivity against effective imaging depth for different focus positions in Figs. 6(f) and 6(g), we have not examined the direct relationship between system sensitivity against OCT SNR in this study. A complicating factor is the use of a common-path interferometer in this, and most other, QME studies [2,4,18,23]. Although a common-path configuration typically has the advantage of improved phase sensitivity [23,48], the reference power cannot be easily adjusted during operation and, hence, it is difficult to selectively adjust the OCT SNR. In addition, the depth-resolved system sensitivity in Fig. 6(g) is likely not purely dependent on OCT SNR, but also depth-dependent translation-induced decorrelation [12,13]. Particularly, using a common-path interferometer, for a sample under a compressive loading, the relative displacement in the sample increases with depth. Chin *et al.* has demonstrated that, using a multiphysics model, the translation-induced decorrelation could degrade displacement sensitivity approximately exponentially regardless of OCT SNR [12]. In general, decoupling and analyzing each of these effects on QME systems sensitivity would be valuable for a future study of QME.

In addition to the relatively wide-field compression used in QME, the analysis of sensitivity and accuracy presented in this framework could also be adapted to assess the performance of other loading methods, such as indentation [54–57]. The stress-localized loading may reduce the artefacts and inaccuracy caused from the irregular surface topology of the tissue sample at the cost of a more limited field-of-view. Lastly, the trade-off between sensitivity and resolution is

highlighted in both Section 4.1 and Section 4.6. With the development of ultrahigh-resolution OCT and strain estimation methods in OCE, this framework provides a quantitative method to optimize the imaging quality. For instance, for a given mechanical loading and OCT system, the trade-off between QME sensitivity and resolution could be a significant criterion to evaluate the performance of prevalent strain estimation methods such as WLS [11] and vector [15] strain estimation, which enables the direct comparison of imaging quality between different methods.

6.　Conclusion

We have presented the first framework to analyze sensitivity and accuracy in QME. We have derived an analytical model for system sensitivity and have shown that system sensitivity is dependent on layer and sample deformation, OCT SNR and signal processing parameters. We have experimentally shown that friction, OCT focus depth, temporal averaging and fitting length of WLS strain estimation directly impact system sensitivity. In addition, we have demonstrated that lubrication can improve accuracy (up to a factor of ~6), while still maintaining high sensitivity (~0.7 kPa) by incorporating temporal averaging. Furthermore, we have showed how feature resolution can be traded off to improve feature sensitivity by incorporating spatial averaging. We believe that our framework can help to better understand the effects of new loading methods, high-resolution OCT systems and signal processing techniques on QME sensitivity and accuracy.

Disclosures. BFK: OncoRes Medical (F, I) and LC: OncoRes Medical (I). The other authors declare that there are no conflicts of interest related to this article.

References

1. K. M. Kennedy, S. Es'haghian, L. Chin, R. A. McLaughlin, D. D. Sampson, and B. F. Kennedy, "Optical palpation: optical coherence tomography-based tactile imaging using a compliant sensor," Opt. Lett. **39**(10), 3014–3017 (2014).
2. K. M. Kennedy, L. Chin, R. A. McLaughlin, B. Latham, C. M. Saunders, D. D. Sampson, and B. F. Kennedy, "Quantitative micro-elastography: Imaging of tissue elasticity using compression optical coherence elastography," Sci. Rep. **5**(1), 15538 (2015).
3. W. M. Allen, K. M. Kennedy, Q. Fang, L. Chin, A. Curatolo, L. Watts, R. Zilkens, S. L. Chin, B. F. Dessauvagie, B. Latham, C. M. Saunders, and B. F. Kennedy, "Wide-field quantitative micro-elastography of human breast tissue," Biomed. Opt. Express **9**(3), 1082–1096 (2018).
4. K. M. Kennedy, R. Zilkens, W. M. Allen, K. Y. Foo, Q. Fang, L. Chin, R. W. Sanderson, J. Anstie, P. Wijesinghe, A. Curatolo, H. E. I. Tan, N. Morin, B. Kunjuraman, C. Yeomans, S. L. Chin, H. DeJong, K. Giles, B. F. Dessauvagie, B. Latham, C. M. Saunders, and B. F. Kennedy, "Diagnostic accuracy of quantitative micro-elastography for margin assessment in breast-conserving surgery," Cancer Res. **80**(8), 1773–1783 (2020).
5. W. J. Hadden, J. L. Young, A. W. Holle, M. L. McFetridge, D. Y. Kim, P. Wijesinghe, H. Taylor-Weiner, J. H. Wen, A. R. Lee, K. Bieback, B. N. Vo, D. D. Sampson, B. F. Kennedy, J. P. Spatz, A. J. Engler, and Y. S. Cho, "Stem cell migration and mechanotransduction on linear stiffness gradient hydrogels," Proc. Natl. Acad. Sci. **114**(22), 5647–5652 (2017).
6. M. S. Hepburn, P. Wijesinghe, L. G. Major, J. Li, A. Mowla, C. Astell, H. W. Park, Y. Hwang, Y. S. Choi, and B. F. Kennedy, "Three-dimensional imaging of cell and extracellular matrix elasticity using quantitative micro-elastography," Biomed. Opt. Express **11**(2), 867–884 (2020).
7. L. G. Major, A. W. Holle, J. L. Young, M. S. Hepburn, K. Jeong, I. L. Chin, R. W. Sanderson, J. H. Jeong, Z. M. Aman, B. F. Kennedy, Y. Hwang, D. W. Han, H. W. Park, K. L. Guan, J. P. Spatz, and Y. S. Choi, "Volume adaptation controls stem cell mechanotransduction," ACS Appl. Mater. Interfaces **11**(49), 45520–45530 (2019).
8. Q. Fang, A. Curatolo, P. Wijesinghe, Y. L. Yeow, J. Hamzah, P. B. Noble, K. Karnowski, D. D. Sampson, R. Ganss, J. K. Kim, W. M. Lee, and B. F. Kennedy, "Ultrahigh-resolution optical coherence elastography through a micro-endoscope: towards in vivo imaging of cellular-scale mechanics," Biomed. Opt. Express **8**(11), 5127–5138 (2017).
9. Q. Fang, B. Krajancich, L. Chin, R. Zilkens, A. Curatolo, L. Frewer, J. D. Anstie, P. Wijesinghe, C. Hall, B. F. Dessauvagie, B. Latham, C. M. Saunders, and B. F. Kennedy, "Handheld probe for quantitative micro-elastography," Biomed. Opt. Express **10**(8), 4034–4049 (2019).
10. Q. Fang, L. Frewer, R. Zilkens, B. Krajancich, A. Curatolo, L. Chin, K. Y. Foo, D. D. Lakhiani, R. W. Sanderson, P. Wijesinghe, J. D. Anstie, B. F. Dessauvagie, B. Latham, C. M. Saunders, and B. F. Kennedy, "Handheld volumetric manual compression-based quantitative microelastography," J. Biophotonics **13**(6), e201960196 (2020).

11. B. F. Kennedy, S. H. Koh, R. A. McLaughlin, K. M. Kennedy, P. R. T. Munro, and D. D. Sampson, "Strain estimation in phase-sensitive optical coherence elastography," Biomed. Opt. Express **3**(8), 1865–1879 (2012).

12. L. Chin, A. Curatolo, B. F. Kennedy, B. J. Doyle, P. R. T. Munro, R. A. McLaughlin, and D. D. Sampson, "Analysis of image formation in optical coherence elastography using a multiphysics approach," Biomed. Opt. Express **5**(9), 2913–2930 (2014).

13. V. Y. Zaitsev, A. L. Matveyev, L. A. Matveev, G. V. Gelikonov, E. V. Gubarkova, N. D. Gladkova, and A. Vitkin, "Hybrid method of strain estimation in optical coherence elastography using combined sub-wavelength phase measurements and supra-pixel displacement tracking," J. Biophotonics **9**(5), 499–509 (2016).

14. V. Y. Zaitsev, A. L. Matveyev, L. A. Matveev, G. V. Gelikonov, A. A. Sovetsky, and A. Vitkin, "Optimized phase gradient measurements and phase-amplitude interplay in optical coherence elastography," J. Biomed. Opt. **21**(11), 116005 (2016).

15. A. L. Matveyev, L. A. Matveev, A. A. Sovetsky, G. V. Gelikonov, A. A. Moiseev, and V. Y. Zaitsev, "Vector method for strain estimation in phase-sensitive optical coherence elastography," Laser Phys. Lett. **15**(6), 065603 (2018).

16. K. M. Kennedy, C. Ford, B. F. Kennedy, M. B. Bush, and D. D. Sampson, "Analysis of mechanical contrast in optical coherence elastography," J. Biomed. Opt. **18**(12), 121508 (2013).

17. A. Ahmad, P. C. Huang, N. A. Sobh, P. Pande, J. Kim, and S. A. Boppart, "Mechanical contrast in spectroscopic magnetomotive optical coherence elastography," Phys. Med. Biol. **60**(17), 6655–6668 (2015).

18. M. S. Hepburn, P. Wijesinghe, L. Chin, and B. F. Kennedy, "Analysis of spatial resolution in phase-sensitive compression optical coherence elastography," Biomed. Opt. Express **10**(3), 1496–1513 (2019).

19. N. Leartprapun, R. R. Iyer, C. D. Mackey, and S. G. Adie, "Spatial localization of mechanical excitation affects spatial resolution, contrast, and contrast-to-noise ratio in acoustic radiation force optical coherence elastography," Biomed. Opt. Express **10**(11), 5877–5904 (2019).

20. M. A. Kirby, K. Zhou, J. J. Pitre, L. Gao, D. Li, I. Pelivanov, S. Song, C. Li, Z. Huang, T. Shen, R. Wang, and M. O'Donnell, "Spatial resolution in dynamic optical coherence elastography," J. Biomed. Opt. **24**(09), 1 (2019).

21. B. Hyle Park, M. C. Pierce, B. Cense, S.-H. Yun, M. Mujat, G. J. Tearney, B. E. Bouma, and J. F. de Boer, "Real-time fiber-based multi-functional spectral-domain optical coherence tomography at 1.3 µm," Opt. Express **13**(11), 3931–3944 (2005).

22. R. K. Wang, S. Kirkpatrick, and M. Hinds, "Phase-sensitive optical coherence elastography for mapping tissue microstrains in real time," Appl. Phys. Lett. **90**(16), 164105 (2007).

23. B. F. Kennedy, R. A. McLaughlin, K. M. Kennedy, L. Chin, A. Curatolo, A. Tien, B. Latham, C. M. Saunders, and D. D. Sampson, "Optical coherence micro-elastography: mechanical-contrast imaging of tissue microstructure," Biomed. Opt. Express **5**(7), 2113–2124 (2014).

24. J. F. Greenleaf, M. Fatemi, and M. Insana, "Selected methods for imaging elastic properties of biological tissues," Annu. Rev. Biomed. Eng. **5**(1), 57–78 (2003).

25. A. Manduca, T. E. Oliphant, M. A. Dresner, J. L. Mahowald, S. A. Kruse, E. Amromin, J. P. Felmlee, J. F. Greenleaf, and R. L. Ehman, "Magnetic resonance elastography: Non-invasive mapping of tissue elasticity," Med. Image Anal. **5**(4), 237–254 (2001).

26. B. F. Kennedy, P. Wijesinghe, and D. D. Sampson, "The emergence of optical elastography in biomedicine," Nat. Photonics **11**(4), 215–221 (2017).

27. J. M. Schmitt, "OCT elastography: imaging microscopic deformation and strain of tissue," Opt. Express **3**(6), 199–211 (1998).

28. R. W. Sanderson, A. Curatolo, P. Wijesinghe, L. Chin, and B. F. Kennedy, "Finger-mounted quantitative micro-elastography," Biomed. Opt. Express **10**(4), 1760–1773 (2019).

29. J. Ophir, I. Céspedes, H. Ponnekanti, Y. Yazdi, and X. li, "Elastography: A quantitative method for imaging the elasticity of biological tissues," Ultrason. Imaging **13**(2), 111–134 (1991).

30. B. F. Kennedy, T. R. Hillman, R. A. McLaughlin, B. C. Quirk, and D. D. Sampson, "In vivo dynamic optical coherence elastography using a ring actuator," Opt. Express **17**(24), 21762–21772 (2009).

31. R. K. Wang, Z. Ma, and S. J. Kirkpatrick, "Tissue Doppler optical coherence elastography for real time strain rate and strain mapping of soft tissue," Appl. Phys. Lett. **89**(14), 144103 (2006).

32. D. C. Ghiglia and M. D. Pritt, *Two-Dimensional Phase Unwrapping: Theory, Algorithms, and Software* (Wiley, 1998).

33. J. W. Goodman, *Statistical Optics*, Wiley Series in Pure and Applied Optics (John Wiley & Sons, Incorporated, 2015).

34. A. C. Chan, E. Y. Lam, and V. J. Srinivasan, "Comparison of Kasai autocorrelation and maximum likelihood estimators for doppler optical coherence tomography," IEEE Trans. Med. Imaging **32**(6), 1033–1042 (2013).

35. P. Beckmann, "Statistical distribution of the amplitude and phase of a multiply scattered field," J. Res. Natl. Bur. Stand. Sect. D Radio Propag. **66D**(3), 231 (1962).

36. E. S. P., and M. G. Kendall, *The Advanced Theory of Statistics* (Griffin, 1947), **110**(2).

37. G. M. P. Van Kempen and L. J. Van Vliet, "Mean and variance of ratio estimators used in fluorescence ratio imaging," Cytometry **39**(4), 300–305 (2000).

38. I. Céspedes, J. Ophir, and M. Insana, "Theoretical bounds on strain estimation in elastography," IEEE Trans. Ultrason. Ferroelectr. Freq. Control **42**(5), 969–972 (1995).

39. S. Makita, F. Jaillon, I. Jahan, and Y. Yasuno, "Noise statistics of phase-resolved optical coherence tomography imaging: single-and dual-beam-scan Doppler optical coherence tomography," Opt. Express **22**(4), 4830–4848 (2014).

40. P. Wijesinghe, D. D. Sampson, and B. F. Kennedy, "Computational optical palpation: A finite element approach to micro-scale tactile imaging using a compliant sensor," J. R. Soc. Interface **14**(128), 20160878 (2017).

41. V. Y. Zaitsev, A. L. Matveyev, L. A. Matveev, E. V. Gubarkova, A. A. Sovetsky, M. A. Sirotkina, G. V. Gelikonov, E. V. Zagaynova, N. D. Gladkova, and A. Vitkin, "Practical obstacles and their mitigation strategies in compressional optical coherence elastography of biological tissues," J. Innov. Opt. Health Sci. **10**(06), 1742006 (2017).

42. J. M. Schmitt, "Restoration of optical coherence images of living tissue using the CLEAN algorithm," J. Biomed. Opt. **3**(1), 66 (1998).

43. S. Kim, M. Kim, H. Shin, and K. Y. Rhee, "Measurement of a nearly friction-free stress–strain curve of silicone rubber up to a large strain in compression testing," Exp. Mech. **58**(9), 1479–1484 (2018).

44. C. Kasai, K. Namekawa, A. Koyano, and R. Omoto, "Real-time two-dimensional blood flow imaging using an autocorrelation technique," IEEE Trans. Sonics Ultrason. **32**(3), 458–464 (1985).

45. P. Wijesinghe, L. Chin, and B. F. Kennedy, "Strain tensor imaging in compression optical coherence elastography," IEEE J. Sel. Top. Quantum Electron. **25**(1), 1–12 (2019).

46. E. Brusseau, J. Kybic, J. F. Déprez, and O. Basset, "2-D locally regularized tissue strain estimation from radio-frequency ultrasound images: Theoretical developments and results on experimental data," IEEE Trans. Med. Imaging **27**(2), 145–160 (2008).

47. P. Wijesinghe, R. A. McLaughlin, D. D. Sampson, and B. F. Kennedy, "Parametric imaging of viscoelasticity using optical coherence elastography," Phys. Med. Biol. **60**(6), 2293–2307 (2015).

48. G. Lan, M. Singh, K. V. Larin, and M. D. Twa, "Common-path phase-sensitive optical coherence tomography provides enhanced phase stability and detection sensitivity for dynamic elastography," Biomed. Opt. Express **8**(11), 5253–5266 (2017).

49. G. Lan, K. V. Larin, S. Aglyamov, and M. D. Twa, "Characterization of natural frequencies from nanoscale tissue oscillations using dynamic optical coherence elastography," Biomed. Opt. Express **11**(6), 3301–3318 (2020).

50. A. Chakraborty, J. C. Bamber, and N. L. Dorward, "Slip elastography: A novel method for visualising and characterizing adherence between two surfaces in contact," Ultrasonics **52**(3), 364–376 (2012).

51. K. Kurokawa, S. Makita, Y.-J. Hong, and Y. Yasuno, "In-plane and out-of-plane tissue micro-displacement measurement by correlation coefficients of optical coherence tomography," Opt. Lett. **40**(9), 2153–2156 (2015).

52. Y. Wang, Y. Wang, A. Akansu, K. D. Belfield, B. Hubbi, and X. Liu, "Robust motion tracking based on adaptive speckle decorrelation analysis of OCT signal," Biomed. Opt. Express **6**(11), 4302–4316 (2015).

53. E. Li, S. Makita, S. Azuma, A. Miyazawa, and Y. Yasuno, "Compression optical coherence elastography with two-dimensional displacement measurement and local deformation visualization," Opt. Lett. **44**(4), 787–790 (2019).

54. Y. Yang, P. O. Bagnaninchi, M. Ahearne, R. K. Wang, and K. K. Liu, "A novel optical coherence tomography-based micro-indentation technique for mechanical characterization of hydrogels," J. R. Soc. Interface **4**(17), 1169–1173 (2007).

55. D. Chavan, J. Mo, M. de Groot, A. Meijering, J. F. de Boer, and D. Iannuzzi, "Collecting optical coherence elastography depth profiles with a micromachined cantilever probe," Opt. Lett. **38**(9), 1476–1478 (2013).

56. Y. P. Huang, Y. P. Zheng, S. Z. Wang, Z. P. Chen, Q. H. Huang, and Y. H. He, "An optical coherence tomography (OCT)-based air jet indentation system for measuring the mechanical properties of soft tissues," Meas. Sci. Technol. **20**(1), 015805 (2009).

57. Y. Qiu, F. R. Zaki, N. Chandra, S. A. Chester, and X. Liu, "Nonlinear characterization of elasticity using quantitative optical coherence elastography," Biomed. Opt. Express **7**(11), 4702–4710 (2016).